Synthesis and antibacterial properties under blue LED light of conjugates between the siderophore desferrioxamine B (DFOB) and an Iridium (III) complex

Aline Faucon [a,b,1], Julien Renault [c,1], Inokentijs Josts [d,e,1,2], Julie Couchot [f], Jean-Luc Renaud [c,g], Françoise Hoegy [a,b], Patrick Plésiat [f,*], Henning Tidow [d,e,*], Sylvain Gaillard [c,*], Gaëtan L.A. Mislin [a,b,*]

[a] CNRS, UMR7242 Biotechnologie et Signalisation Cellulaire, 300 Boulevard Sébastien Brant, F-67412 Illkirch, Strasbourg, France
[b] Université de Strasbourg, Institut de Recherche de l'Ecole de Biotechnologie de Strasbourg (IREBS), 300 Boulevard Sébastien Brant, F-67412 Illkirch, Strasbourg, France
[c] Normandie University, LCMT, ENSICAEN, UNICAEN, CNRS, 6 Bd du Maréchal Juin, 14050 Caen, France
[d] The Hamburg Advanced Research Center for Bioorganic Chemistry (HARBOR), 22761 Hamburg, Germany
[e] Department of Chemistry, Institute for Biochemistry and Molecular Biology, University of Hamburg, 22761 Hamburg, Germany
[f] Université de Franche-Comté, UMR6249 CNRS Chrono-environnement, F-25000 Besançon, France
[g] Sorbonne Université, CNRS, Institut Parisien de Chimie Moléculaire, UMR 8232, 75005 Paris, France

ARTICLE INFO

ABSTRACT

The decline of antibiotics efficacy worldwide has recently reached a critical point urging for the development of new strategies to regain upper hand on multidrug resistant bacterial strains. In this context, the raise of photodynamic therapy (PDT), initially based on organic photosensitizers (PS) and more recently on organometallic PS, offers promising perspectives. Many PS exert their biological effects through the generation of reactive oxygen species (ROS) able to freely diffuse into and to kill surrounding bacteria. Hijacking of the bacterial iron-uptake systems with siderophore-PS conjugates would specifically target pathogens. Here, we report the synthesis of unprecedented conjugates between the siderophore desferrioxamine B (DFOB) and an antibacterial iridium(III) PS. Redox properties of the new conjugates have been determined at excited states and compared to that of an antibacterial iridium PS previously reported by our groups. Tested on nosocomial pathogen *Pseudomonas aeruginosa* and other bacteria, these conjugates demonstrated significant inhibitory activity when activated with blue LED light. Ir(III) conjugate and iridium free DFOB-2,2′-dipyridylamine ligands were crystallized in complex with FoxA, the outer membrane transporter involved in DFOB uptake in *P. aeruginosa* and revealed details of the binding mode of these unprecedented conjugates.

1. Introduction

Bacterial resistance to antibiotics has become a major global health challenge for humans, animals and the environment. In this context, new therapeutic strategies to regain upper hand on critical pathogens are more than ever awaited.[1–2] Along with vaccines,[3] bacteriophages,[4] and ultrasounds,[5] light-based technologies are considered as potential candidates to combat drug resistant microorganisms. The potential of light to destroy living cells has been known for more than a hundred years,[6] opening perspectives in the treatment of cancer as well as infectious diseases.[7] First attempts to use UV in therapeutics however failed because of the toxicity of these high energy irradiations on human tissues.[7–8] Shift of the excitation spectrum to visible or even more suitable infra-red wavelengths as achieved with photosensitizers (PS) proved to be a safer option.[7,9] Organometallic compounds showing promising potential as antibacterials were progressively evaluated.[10–12] Depending on the metal and its organic counterpart, organometallics can be activated with visible light and generate reactive oxygen species

---

(ROS). Nonetheless, the deleterious effects of both the metal and the ROS on human cells preclude the use of such PS in patients. Improving the delivery to bacteria has rapidly emerged as a prerequisite in antibacterial PDT. Because of its poor permeability, the outer membrane of Gram-negative bacteria tends to impair the penetration of large and/or hydrophobic molecules including metal complexes.[13] To bypass this semipermeable permeability barrier, nutrient uptake systems can be used as gates in the so-called Trojan Horse strategy. Iron is an interesting bait since this essential metal is not metabolically substitutable. Moreover, iron uptake systems in bacteria differ significantly from the iron import processes of mammalian cells. Evolution has endowed bacteria with very efficient iron acquisition mechanisms,[14–15] most of which rely on secretion and recapture of small chelating metabolites named siderophores (from the Greek *sídēros*, iron; and *phérein*, carrying). In the extracellular medium, these molecules scavenge iron(III).[15] In Gram-negative bacteria, the corresponding ferric complexes are recognized by specific outer membrane transporters (OMT),[16] and then translocated into the periplasmic space thanks to the energy provided by the TonB machinery.[17] The ferri-siderophore complexes are further dissociated through a Fe(III) to Fe(II) reductive process that most often goes along with chemical modification of the siderophore (acylation, hydrolysis, etc…).[18] Depending on the siderophore but also on the bacterial species considered, the imported iron is released either in the periplasm or in the cytoplasm. In this latter case, the ferric-siderophores are specifically translocated across the inner membrane by permeases or ABC proteins.[18] Some siderophores are recycled and reexported to the extracellular medium.[19–20] Highlighting the potential of Trojan horse strategy, bacterial iron uptake systems can be hijacked by natural products such as the sideromycines, which consist of an antibiotic moiety coupled with a siderophore. Different studies demonstrated that the sideromycines albomycines and microcine E492 have higher antibacterial activities than their non-vectorized antibiotic parts.[21–22] These findings elicited a scientific interest for the synthesis of artificial sideromycines, which culminated with the marketing of cefiderocol, the first approved antibiotic-siderophore conjugate.[23] Although the vectorization of organic antibacterial compounds is the matter of a booming literature,[24–27] siderophores have been much more scarcely reported as cargos for organometallic payloads. Conjugates between ruthenium(II)

and desferrioxamine B (DFOB) derivatives (compound **1** is given as an example),[28] and platinum(IV) and an enterobactin analogue (conjugate **2**) have been described.[29] More recently, conjugate **3** composed of ruthenium(IV) and a catechol siderophore was shown to promote the intrabacterial conversion of a moxifloxacin prodrug.[30] (Figure 1). To some extent, a selectivity for bacterial *versus* eukaryotic cells was noted in *in vitro* experiments.[28–29] Even if the aforementioned vectorized metal complexes failed to find PS applications, these examples support the notion that siderophores can be used as cargo to deliver organometallics into bacteria. Organometallic PS based on ruthenium have been particularly studied in the frame of antibacterial PDT,[31–33] while other metals complexes were rarely evaluated. Among other noble metals, cyclometallated iridium(III) complexes possess some assets for the development of new PS able to generate ROS, such as (i) a high photostability due to their hexacoordination mode limiting nucleophilic attacks, (ii) an easy tunability of the photophysical properties in the visible spectrum, and (iii) oxidative potentials at excited state compatible for the generation ROS.

P. aeruginosa is a Gram-negative bacterium involved in severe lung infections and also responsible for infections that are difficult to treat in the case of deep wounds and extensive burns. These skin infections are therefore particularly interesting targets for PDT given the good accessibility to light and the ease of administration of PS (topical). As proof of concept for the potential vectorization of iridium(III) complexes, our groups synthesized a bis-cyclometallated iridium(III) with 2-phenylisoquinoline (piq) and coordinated to a biotin-functionalized 2,2′-dipyridylamine derivatives as ancillary ligand. This bioconjugated iridium **4** revealed itself encouraging PS as an enhanced antibacterial on both planktonic and sessile *P. aeruginosa* cells under blue LED light was clearly noted (Figure 1).[34] Unfortunately, the biotin uptake systems targeted by this approach are not present in all bacterial species and strains,[35] siderophores therefore appearing to be more versatile cargos.

DFOB **7**, a tris-hydroxamate siderophore excreted by *Streptomyces pilosus*, is able to chelate iron(III) to form stable ferric complexes (pFe = 26.5).[36] Albeit not produced by *P. aeruginosa*, DFOB can be scavenged by the bacterium as an auxiliary siderophore to fulfill its needs in iron in specific starving environments.[37] Ferric DFOB is recognized by FiuA, an OMT dedicated to the import of ferrichrome, and by FoxA that
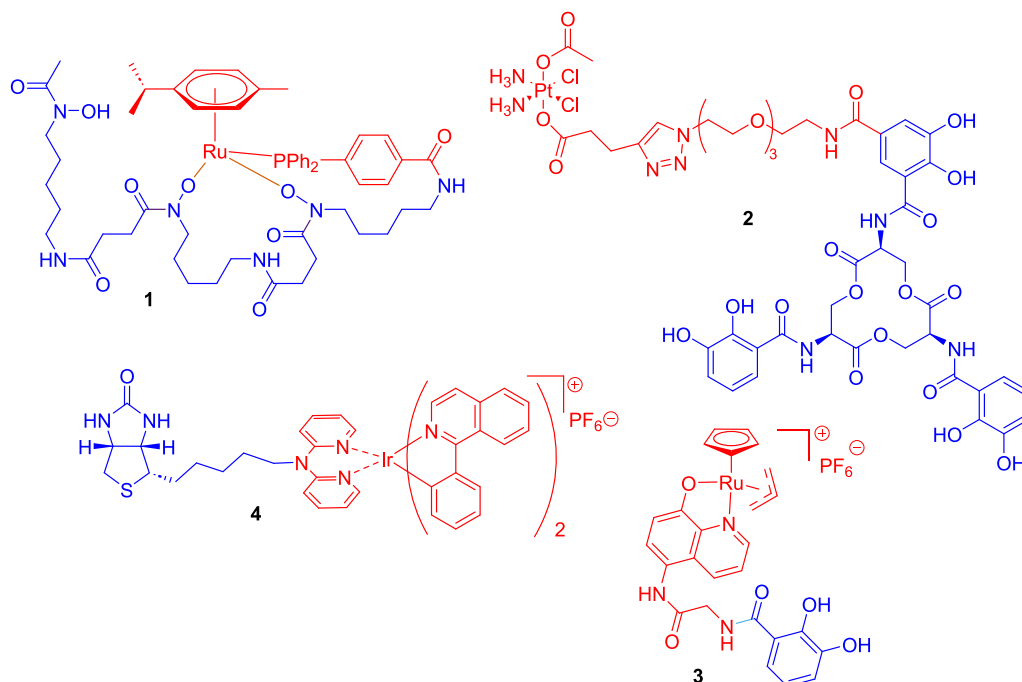
Figure 1. Examples of vectorized organometallic compounds **1** to **4**. The vector moieties are colored in blue. The linkers and the metal complexes are colored in red.

specifically shuttles DFOE (also called nocardamin).[38] More recently the OMT FpvB was also demonstrated to transport DFOB.[38–39] In the Fox upake system, once in the periplasmic space, the ferric DFOB induces expression of the FoxA-encoding gene via a mechanism implying the sigma and anti-sigma factors FoxI and FoxR, respectively.[37] The release of iron from the siderophore was shown to depend on oxidoreductase FoxB activity.[40] The fate of both iron and the siderophore after dissociation remains unknown in *P. aeruginosa*. Altogether these data prove that DFOB actively enter *P. aeruginosa* cells and may potentially serve to shuttle PS into this pathogen. In this context, we synthetized conjugates coupling DFOB and iridium(III) complexes. The biological properties of these conjugates against *P. aeruginosa* and other bacterial pathogens were assessed in the presence and absence of blue LED light, respectively. Moreover, co-crystallization with the OMT FoxA showed that the DFOB derivatives bind to FoxA and revealed their binding site/mode.

2. Results and discussion

2.1. Synthesis of conjugates between DFOB and Ir(III) complexes

As mentioned previously, iridium(III) complexes can acquire interesting antimicrobial activities once conjugated with biotin (compound **4**, Figure 1).[34] Therefore, the conjugation of iridium(III) complexes, cyclometallated to 2-phenylisoquinoline (piq) and bearing 2,2′-dipyridylamine (dpa) derivatives as ancillary ligand, as PS, combined with our approach with DFOB appeared obvious. Loading of DFOB with Ir(III) requires *N*-functionalized dpa ligands able to be conjugated with the siderophore. Since envisioned Ir(III) complex is a bulky molecule, two spacer arms with two different lengths were evaluated in order to assess a possible impact of steric hindrance on the biological activity. For the short spacer, commercially available 2,2-dipyridylamine **5** was converted into the carboxylate **6** according a published procedure (72 % yield over two steps).[41–42] Commercially available DFOB mesylate **7** was then reacted with carboxylate **6** in the presence of *N*-(3-dimethylaminopropyl)-*N*′-ethylcarbodiimide hydrochloride (EDCI.HCl) and of Hünig base. The expected DFOB **8** functionalized with a dpa was isolated in 91 % yield (Scheme 1).

For the long spacer, on one hand, the commercially available amine **11** was coupled to carboxylate **6** with EDCI.HCl in the presence of Hünig base. The expected azide-functionalized dpa **12** was isolated in 77 % yield. On the other hand, DFOB mesylate **7** was treated with propargyl chloroformate in the presence of Hünig base in hot *N,N*-dimethylformamide (DMF) leading to the expected propargyl-DFOB **13** isolated with 86 % yield. A copper-mediated Azide-Alkyne Cycloaddition (CuAAC) between **12** and **13**,[43–45] in the presence of sodium ascorbate, provided the DFBO-dpa derivative **14** in 44 % isolated yield (Scheme 2).

Ligands **8** and **14** were then coordinated to cyclometallated iridium metal center in the presence of the dimer **9** in a CH$_2$Cl$_2$:MeOH 2:1 mixture at room temperature for 24 h. Due to the close polarity between targeted conjugates and the DFOB-functionalized dipyridylamine derivatives **8** and **14**, usual silica gel chromatography failed to furnish pure products in our hands. Thanks to their different molecular weight and steric hindrance, the conjugates **10** and **15** were satisfactorily purified using Size Exclusion Chromatography (*SEC*) with 88 % isolated yield. Of note, this purification allowed also to recover the excess iridium dimer **9** pure enough to be reused for another synthesis (Scheme 3).

Compounds **10** and **15** are the first conjugates to be reported so far between a siderophore and an Ir(III) complex. We therefore investigated whether the presence of this chelating entity could impact photophysical and redox properties of the iridium complex necessary for the antibacterial activity through photoactivation.

2.2. Photophysical and redox properties of DFO-Ir(III) conjugates

Once conjugates **10** and **15** in hands, photophysical properties of the iridium frameworks were characterized and compared to benchmark
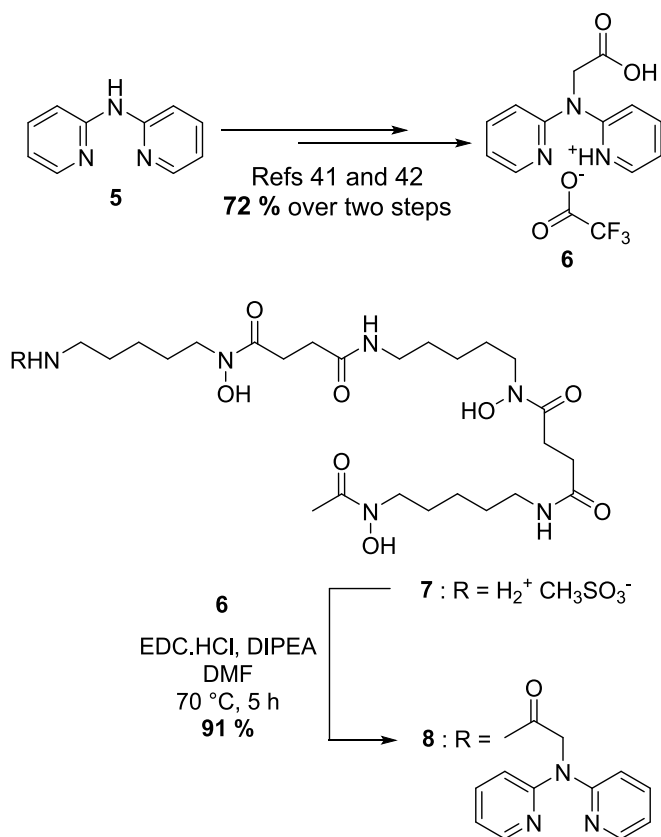
Scheme 1. Synthesis of DFOB-dpa ligand **8**.
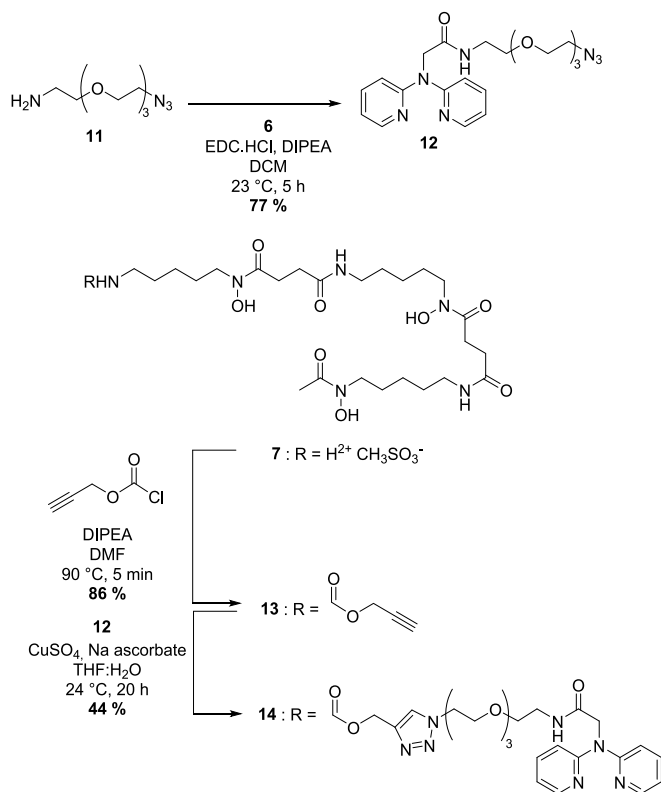
Scheme 2. Synthesis of DFOB-dpa ligand **14**.

Scheme 3. Synthesis of DFOB-Ir(III) conjugates **10** and **15**. Structure of the benchmark Ir(III) complex **16**.
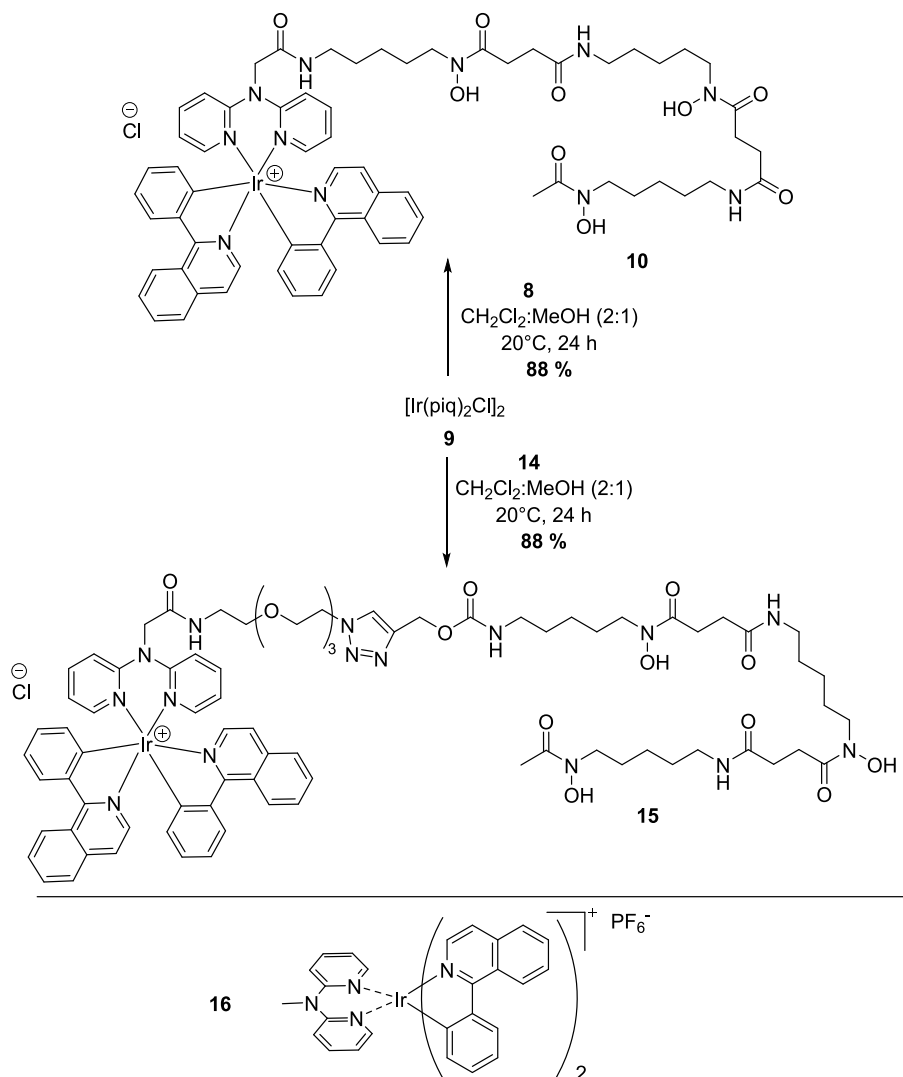
complex **16** cyclometallated to piq and coordinated to *N*-methyl dpa ancillary ligand (Scheme 3) that have been previously synthesized and characterized in our group (Table 1).[34] The UV–Visible spectra of the iridium complexes **10**, **15** and **16** were recorded in dichloromethane at 298 K (Figures S19 to S21). Then, emission spectra, lifetime and photoluminescence quantum yield of the iridium complexes **10**, **15** and **16** were recorded in degassed dichloromethane at 298 K. All the photophysical data were summarized in Table 1.

Similarly to complex **16**,[34] conjugates **10** and **15** exhibited intense absorption in the UV region from 250 nm to 360 nm (ε of around 35 000 $M^{-1} \cdot cm^{-1}$ at 294 nm and around 15 500 $M^{-1} \cdot cm^{-1}$ at 343 nm) and a lower absorption band in the blue region with local absorption maxima at 438 nm (ε of around 4800 $M^{-1} \cdot cm^{-1}$).

For the emission properties, no drastic modification of the maximum emission wavelengths of compounds **10** and **15** was observed compared to complex **16** with values in the error range at around 640 nm. Then, a decrease by a factor of 2 was noticed for the photoluminescent quantum yield (Φ) of the conjugates **10** and **15** ($\Phi = 5.0$ and 5.9 %, respectively) compared to the reference (9.9 % for complex **16**). Considering the decay time of the emission, all these complexes exhibited monoexponential decays with close life time of hundreds of nanoseconds order, which is typical for iridium(III) complexes.[46] Then, to evaluate the potential ROS photogeneration of the newly synthesized conjugates **10** and **15**, voltammograms were recorded in deaerated acetonitrile to firstly determine redox potential at ground state (Figures S22 to S24, Table 2).

Reversible oxidation waves, attributed to the oxidation couple $E_{ox}([Ir^{IV}]/[Ir^{III}])$,[47–49] were observed at values of 1.17 and 1.21 V vs. Ag/AgCl for bioconjugates **10** and **15**. Of note, complex **16** exhibited a close oxidation potential value equal to 1.22. On the other hand, semi reversible reductive processes attributed to the reduction of the diamine ligand were observed at values of −1.61 and −1.62 V for the conjugates

Table 1
Photophysical data of compounds **10**, **15** and **16**.

Complex	Absorption[a]	Emission[b]		
	λ_{abs} (nm)/ (ε in x10^3 $M^{-1} \cdot cm^{-1}$)	λ_{em} (nm)	τ (ns)	Φ (%)
10	294 (33.6), 343 (15.9), 386 (7.6),438 (4.7), 473 (2.3)	639	857	5.0
15	294 (33.6), 343 (15.4), 386 (7.5),438 (4.9), 473 (2.6)	641	539	5.9
16	294 (37.9), 343 (15.5), 386 (7.3),438 (4.8), 473 (2.4)	639	680	9.9

[a] In dichloromethane solution. [b] In deaerated dichloromethane solution c = 1.10^{-5} M.

Table 2

Redox potentials at ground and excited states, and photoactivation energy of complexes **10**, **15** and **16**.

Complex	$E_{ox}([Ir^{IV}]/[Ir^{III}])$	$E_{red}([Ir^{III}]/[Ir^{II}])$	E_{00} (eV)	$E_{ox}([Ir^{IV}]/[Ir^{III}]*)$	$E_{red}([Ir^{III}]*/[Ir^{II}])$
10	1.17	−1.61	1.94	−0.77	0.33
15	1.21	−1.62	1.93	−0.72	0.31
16	1.22	−1.34	1.94	−0.72	0.60

Redox potentials at excited state were approximated as follow: [a] $E_{ox}([Ir^{IV}]/[Ir^{III}]*) = E_{ox}([Ir^{IV}]/[Ir^{III}]) - E_{00}$. [b] $E_{red}([Ir^{III}]*/[Ir^{II}]) = E_{red}([Ir^{III}]*/[Ir^{II}]) + E_{00}$.

10 and **15**. Here, a noticeable difference can be noted with the benchmark complex **16** possessing a reduction potential of −1.34, but can be attributed to the nature of the *N*-substituent of the dpa derivative that might modified the electronic density in the NˆN ligand.[47–49] Having the redox properties at ground state in hands, approximation of the redox potential at the excited state, i.e. $[Ir^{IV}]/[Ir^{III}]*$ and $[Ir^{III}]*/[Ir^{II}]$, was undertaken using the λ_{em} of the compounds for the determination of the photoactivation energy E_{00}.[50] Interestingly, the oxidation potentials $E_{ox}([Ir^{IV}]/[Ir^{III}]*)$ of compounds **10** and **15** were estimated to be in the same range than complex **16** (− 0.77 and − 0.72 V compared to − 0.72 V, respectively). In regard to the reduction potential of dioxygen into the reactive oxygen species $O_2^{\cdot-}$[51] having a value of $E_{red}(O_2/O_2^{\cdot-}) = - 0.75$ V vs SCE, the $E_{ox}([Ir^{IV}]/[Ir^{III}]*)$ of conjugates **10** and **15** appeared compatible for the photogeneration of this kind of ROS. In addition, the previously observed antibacterial activity of complex **16** possessing similar photophysical and electrochemical properties encouraged us to perform antimicrobial assays on *P. aeruginosa* and other bacterial pathogens.[34]

2.3. Antibacterial properties against P. aeruginosa

The minimal inhibitory concentrations (MICs) of complexes were determined on wild-type reference *P. aeruginosa* strain PAO1 and related mutants (Table S1). The bacteria were grown in parallel in Mueller-Hinton broth (MH, Becton, Dickinson and Company, Sparks, USA) and a same batch of MH pre-treated with Chelex® to remove most of its iron (<30 μg/L), according to international guidelines for testing siderophore antibiotics.[52] Susceptibility levels of strain PAO1 to conjugates **10** and **15** were assessed in the dark and upon blue LED light (473 nm; 388 μW/cm²; Figure S25). Preliminary experiments confirmed that the LED blue light used in the laboratory had no effects by itself on strain PAO1 growth (data not shown). As supplementary controls, iridium free DFOB-dpa **8** was also tested along with non-vectorized Ir(III) complex **16**. As recalled above, DFOB is not produced by *P. aeruginosa* but when present in the extracellular medium, the siderophore induces expression of dedicated OMTs FoxA and FiuA.[37–38] To investigate the involvement of these OMTs and several other iron transport mechanisms in the uptake of our Ir(III) conjugates, a series of PAO1 deletion mutants were included in the susceptibility tests, namely PAS283 (Δ*pchA*Δ*pvdF*), a derivative unable to produce the endogenous siderophores pyochelin and pyoverdine, PAS534 (Δ*pchA*Δ*pvdF*Δ*foxA*), PAS535 (Δ*pchA*Δ*pvdF*Δ*fiuA*), and PAS536 (Δ*pchA*Δ*pvdF*Δ*fiuA*Δ*foxA*). Confirming previous results,[34] the non-vectorized Ir(III) complex **16** did not exhibit inhibitory activity on the parental strain PAO1 in the dark (MIC≥128 mg/L) (Table 3). In strong contrast, but consistent with the lack of a siderophore moiety in the molecule, its MICs dropped more than 1,024-fold under blue LED light activation (between ≤ 0.06 and 0.12 mg/L) on both wild-type (proficient) and iron-transport deficient strains. DFOB-dpa **8** which does not contain Ir(III) was logically found to be devoid of antibacterial activity whatever the strains and illumination conditions used. The DFOB-Ir(III) conjugates **10** and **15** gave similar results, being inactive in the dark but demonstrating an interesting efficiency (2 < MIC<8 mg/L) under blue LED light, on all the strains. However, these activities were from 12.5- to ≥ 80-fold less than those of the

non-vectorized Ir(III) complex **16** when compared on a molar basis (Table S2). Furthermore, the MICs of **10** and **15** were not significantly affected by the lack of iron transport systems including FoxA and FiuA (compare results for PAO1 and PAS536, Table 3), or iron depletion of the nutrient broth (compare with results into brackets, Table 3).

2.4. Antibacterial properties against other pathogens

Additional experiments were performed to check the antibacterial activities of **16** and **10** on two other wild-type reference Gram-negatives, namely *Escherichia coli* ATCC25922 and *Acinetobacter baumannii* CIP 70.10, and a Gram-positive species, *Staphylococcus aureus* ATCC 29213, used as a control species devoid of outer membrane (Table S3). In contrast to the *P. aeruginosa* strain PAO1, these species were inhibited by non-conjugated compound **16** in the dark (MICs ranging from 0.5 mg/L for *S. aureus* to 32 mg/L for *E. coli* in iron-repleted MH broth) while showing a similar or lower susceptibility (from ≤ 0.06 to 1 mg/L) upon blue light excitation (0.12 mg/L for PAO1). Only *S. aureus* displayed some susceptibility to conjugate **10** in the dark (8 mg/L in iron-repleted MH). Under blue light exposure, MIC values of **10** turned out to be rather similar for all the Gram-negatives both in high- and low-iron media (from 0.5 to 8 mg/L), however being much higher than those for *S. aureus* (≤0.06 mg/L). Taken together, these results confirm the protective role played by the outer membrane of Gram-negatives against large and hydrophobic molecules.[13] They also highlight a nonspecific sensitization (i.e., independent from the expression of siderophore receptors FoxA and FiuA) of these Gram-negative bacteria to iridium complexes upon iron depletion, visible with both the conjugated and non-conjugated compounds. The mechanisms underlying such increase in susceptibility are still unclear and warrant further investigations.

2.5. Interaction of DFO derivatives with FoxA outer membrane transporter

These biological experiments suggest that vectorization of our Ir(III) complex by DFO offered no added value compared with the non-vectorized molecules. The previously reported antibacterial activity of biotin complex **4** (Figure 1) on *P. aeruginosa* in the dark, might be due to the intrinsic toxicity of the metal assimilated by the bacteria.[34] Supporting this assumption, the same complex vectorized by a sugar moiety recognized by extracellular lectins of *P. aeruginosa* was active under blue LED light but not in the dark. Since DFOB conjugates **10** and **15** present similar characteristics, the ability of these conjugates to actively enter bacteria should be questioned. ^{55}Fe uptake assays have not been able to demonstrate this uptake. These experiments led to very high signal-to-noise ratios, probably due to the precipitation of the corresponding iron complexes. The first lock to gain access to the bacterial inner space

Table 3

Susceptibility levels of *P. aeruginosa* strains to iridium conjugates.

	MIC (mg/L) under blue LED light exposure				
Molecules	PAO1	PAS283	PAS534	PAS535	PAS536
8	≥ 128 (≥128)	≥ 128 (≥128)	≥ 128 (≥128)	≥ 128 (≥128)	≥ 128 (≥128)
16	0.12 (≤0.06)	≤ 0.06 (0.12)	≤ 0.06 (0.12)	≤ 0.06 (0.12)	≤ 0.06 (0.12)
10	4(2)	4(2)	4(2)	8(2)	4(2)
15	8(4)	8(4)	4(4)	8(8)	8(8)

Bacterial strains were grown in Mueller Hinton broth and in iron-depleted Mueller Hinton broth (values into brackets) at 35 °C±2 for 18 h ± 2 in the presence of DFOB siderophore **8**, Ir(III) complex **16**, or DFOB-Ir(III) conjugates **10** and **15**, both in the dark (controls) and under blue LED light at 388 μW/cm². Individual MIC values correspond to the modal of three independent experiments. Mutants PAS283, PAS534, PAS535 and PAS536 lack the genes *pvdF/pchA*, *pvdF/pchA/fiuA*, *pvdF/pchA/foxA*, and *pvdF/pchA/fiuA/foxA*, respectively. [1]In the dark, all MIC values were ≥128 mg/L and are not presented here.

is the recognition of the siderophore moiety by specific OMT. In this context, investigations of the interactions between some of our DFO derivatives and FoxA OMT can help in the comprehension of biological results.

In order to investigate their binding mode, we co-crystallized the outer membrane transporter FoxA with compounds **8**, **10**, **14**, and **15** as previously described for the siderophores DFOB, nocardamine (NOCA), and bisucaberin.[38,53–54] While no crystals were obtained for compound **10**, compounds **8**, **14** and **15** resulted in diffracting protein crystals. The structure of FoxA in complex with compound **8** was determined to 2.22 Å resolution and showed good electron density for the entire ligand (Figure 2, Figures S26 and S27, Table S4). The siderophore moiety of the ligand occupies the same binding site as ferrioxamine B as compared with the previously determined structure of FoxA bound with ferrioxamine B. Additionally, we could observe extra density for the 2,2′-dipyridylamine moiety within the binding pocket. The 2,2′-dipyridylamine moiety of the ligand is seemingly stabilized by cation-pi interactions with Y458 and W503 through ammonium ions in the binding pocket (Figure 2).

The co-crystal structure with compound **14** (determined to 2.48 Å resolution) shows a very similar binding mode for the siderophore part of the molecule. The 2,2′-dipyridylamine moiety (compared to compound **8**) protrudes closer to W503 and one of the pyridyl rings occupies the space of ammonium ion adjacent to W503 (Figure 2). The pi-cation interactions of the second pyridyl ring with Y458 through an ammonium ion are still maintained. The extended linker coupling the siderophore moiety with the 2,2′-dipyridylamine group is less defined in the electron density, indicating some degree of disorder within the crystal (Figures S26 and S27).

For the Ir(III)-bound compound **15** we were not able to obtain diffraction data of sufficient quality to fully refine the ligand. However, additional electron density in the siderophore binding pocket of FoxA after molecular replacement confirms binding of this compound. Anomalous difference maps suggest that the cyclometallated Ir(III)-containing moiety is protruding towards the outside of the siderophore moiety (Figure S28).

3. Conclusion

The present work describes the synthesis of DFOB analogues **8** and **14** obtained in good yield by hexadentate DFOB siderophore and bidentate 2,2′-dipyridylamine. To our knowledge **8** and **14** are the first examples of DFOB exhibiting both oxygen and nitrogen atoms as chelating moieties. Importantly, the iron chelating functions of DFOB did not interfere for the complexation of the cyclometallated Ir(III) by the 2,2′-dipyridylamine during the synthesis of conjugates **10** and **15**.

The difficulties encountered during isolation of the unprecedent DFOB-Ir(III) complex conjugates **10** and **15** with usual stationary phases, i.e. silica gel, have been tackled by using the Size Exclusion Chromatography (*SEC*). Importantly, the siderophore cargo did not affect the photophysical properties of the iridium(III) payload and both conjugates **10** and **15** shown ROS photogeneration under blue LED light irradiation. This ROS production could be correlated with an impressive antibacterial effect on *P. aeruginosa*. However, in the presence or in absence of light, MICs assessed on *P. aeruginosa* PAO1 mutated in the expression of the OMTs FiuA and FoxA were not higher than the non-vectorized Ir(III) complex **16**. Similar results were obtained on other pathogenic bacteria (*A. baumanni*, *E. coli* and *S. aureus*). This result suggests that conjugation with DFOB does not enhance the antibacterial effect of the Ir(III) derivative, which raises several hypotheses. Since the OMT is the first lock to access the inside of the bacterium, altered recognition between the transporter and the conjugated siderophore could explain the observed result. The three-dimensional structure of the OMT FoxA was previously solved in complex with ferric DFOB, nocardamine (DFOE) and other related molecules.[38,53–54] The structures of ferric DFOB derivatives **8** and **14** were here determined in complex with FoxA (PDB 8RM3 and PDB 8RMI). Although obtained at lower resolutions, the three-dimensional structure of the ferric conjugate **15** in complex with FoxA shows that such an organometallic conjugate remains capable of binding the targeted OMT. This observation raises questions about the fate of the conjugate after its recognition and the transport capacity of the OMT for these unprecedented organometallic conjugates. Investigations are currently underway to determine if the transfer to the periplasm is possible. Even though siderophores can serve as cargo for charged and bulky payloads, the literature shows that the nature of the siderophore often prevails in the effectiveness of a Trojan Horse strategy. In a first approach, DFOB was selected as siderophore vector since it is used by many pathogens, including *P. aeruginosa*. However, in the specific case of organometallic payloads catechol vectors appears to be more promising in the light of recent literature releases,[29–30] and might be the better option to improve the impact of our strategy on Gram-negative bacteria. The combination of the specific delivery of an organometallic photosensitizer by a siderophore vector and light-triggered antimicrobial activity should indeed open up new therapeutic perspectives against problematic bacterial pathogens.

4. Experimental

4.1. Chemistry

4.1.1. Chemicals

Compounds **6** was prepared according previously described
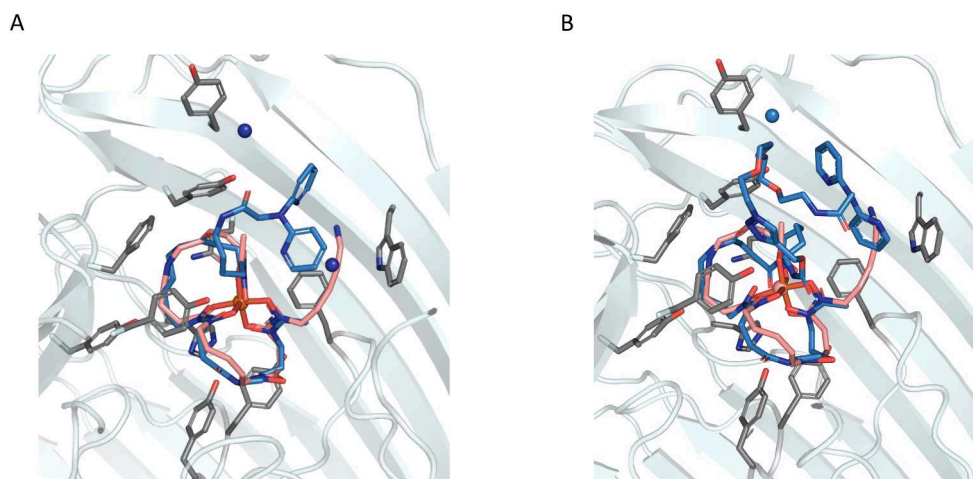
Figure 2. Superposition of FoxA crystal structures in complex with DFOB (pdb: 6I96) (salmon) with (A) ligand **8** (blue) and (B) ligand **14** (blue).

protocols.[41–42] Compound **16** was prepared according a previously described protocol.[34] Iridium(III) chloride was bought from Alfa aesar. Coumarin C6 was purchased from Sigma Aldrich. All solvents were purchased from Carlo Erba. All reactions were carried out under argon (technical quality, Linde). Solvents used were of analytical grade purity (>99 %). When necessary, solvents and bases were purchased extra-dry. All other chemicals were obtained from commercial suppliers and were used as received, unless otherwise stated.

4.1.2. Chromatographic analysis and purification

All reactions were monitored by thin-layer chromatography (TLC) using *Merck* precoated silica gel 60F^{254} (0.25 mm). TLC are visualized using UV (254 nm/365 nm, *Vilber Lourmat*, VL-4LC) and/or using classical revelation mixtures (sulfuric vanillin, potassium permanganate, ninhydrin reagent). Iron chelating compounds were also detected on TLC using a 2 % hydromethanolic solution of FeCl$_3$. Before chromatographic purifications, reaction mixtures were adsorbed on silica gel (60–200 µm, VWR Chemicals). Chromatographic purifications were performed on a Selekt (*Biotage*) purification device using PuriFlash® pre-packed silica gel columns (Interchim, Montluçon, France). Size exclusion chromatography columns were carried on Bio-Beads S-X3® resin composed of styrene divinylbenzene beads, 3 % cross-linkage and 40–80 µm bead size. Compounds were eluted using CH$_2$Cl$_2$.

4.1.3. Spectroscopic analysis

NMR spectra were recorded on Bruker Avance 400 (^{1}H: 400 MHz, ^{13}C: 100 MHz), Avance 500 (^{1}H: 500 MHz, ^{13}C: 125 MHz), Avance III 500 (^{1}H: 500 MHz, ^{13}C: 125 MHz) or Neo600 (^{1}H: 600 MHz, ^{13}C: 151 MHz) using the residual non-deuterated solvent as reference. The chemical shifts (δ) and coupling constants (J) are expressed in ppm and Hertz respectively. Multiplicity is indicated as follow: s for singlet, d for doublet, t for triplet, q for quadruplet, quint for quintuplet and m for a multiplet. The letter "b" before the multiplicity indicates a broaden signal. Chemical shifts (δ) of carbon^{13}C) NMR spectra are reported in ppm relative to CDCl$_3$ unless stated otherwise Mass spectra were recorded in the *Service Commun d'Analyses* (SCA) *de la Faculté de Pharmacie de l'Université de Strasbourg* LC/BRMS conditions: Analytical RP-HPLC-MS was performed using a LC 1200 Agilent with quadrupole-time-of-flight (QTOF) (Agilent Accurate Mass QToF 6520) with a Zorbax Agilent C18-column (C18, 50 mm x 2.1 mm; 1.8 µm) using the following parameters: The solvent system: A (acetonitrile + 0.05 % formic acid) and B (H$_2$O+0.05 % formic acid); Gradient (Tmin,(%B)): T0 (98 %), T4(0 %), T8(0 %), T8.1(98 %). Flow rate of 0.5 mL/min; Column temperature: 40 °C; DAD scan from 190 nm to 700 nm. Ionization mode: ESI$^+$. LC/HRMS conditions: Analytical RP-HPLC-HRMS was performed using a LC 1200 Agilent with quadrupole-time-of-flight (QToF) (Agilent Accurate Mass QToF 6520) with a Zorbax Agilent C18-column (C18, 50 mm x 2.1 mm; 1.8 µm) using the following parameters: The solvent system: A (acetonitrile + 0.05 % formic acid) and B (H$_2$O+0.05 % formic acid); Gradient: (Tmin,(%B)): T0 (98 %), T8(0 %), T12.5(98 %), T12.6 (98 %), T13(98 %). Flow rate of 0.5 mL/min; Column temperature: 40 °C; DAD scan from 190 nm to 700 nm. Ionization mode: ESI$^+$. For HRMS, the calculated and the found mass correspond to M. Original ions repartition could be found in ions table and simulation given in ESI. HRMS analysis of compounds **10** and **15** were performed by the LCMT analytical service.

4.1.4. N^1-(5-(2-(di(pyridin-2-yl)amino)acetamido)pentyl)-N^1-hydroxy-N^4-(5-(N-hydroxy-4-((5-(N-hydroxyacetamido)pentyl)amino)-4-oxobutanamido)pentyl)succinimide (8)

To a solution of **7** (405 mg, 0.58 mmol, 1 eq.) and acid **6** (200 mg, 0.58 mmol, 1 eq.) in DMF (6 mL), was added DIPEA (151 mg, 0.19 mL, 1.17 mmol, 2 eq.). The mixture was stirred at 70 °C for 30 min, then EDC.HCl (236 mg, 1.24 mmol, 2,1 eq.) was added. The reaction mixture was stirred at 70 °C for 5 h, then adsorbed on silica and purified by chromatography on silica gel column (gradient MeOH with 0.5 % H$_2$O in DCM, 0 % to 30 %) to give the expected product **8** isolated as a white solid (401 mg, 0.52 mmol, yield: 91 %). ^{1}H NMR (500 MHz, DMSO-d_6): δ 9.66 (s, 1H), 9.61 (s, 2H), 8.27 (d, *J*=3.7 Hz, 2H), 7.82 (t, *J*=5.8 Hz, 1H), 7.77 (t, *J*=5.7 Hz, 2H), 7.65 (t, *J*=7.5 Hz, 2H), 7.22 (d, *J*=8.4 Hz, 2H), 6.96 (t, *J*=5.7 Hz, 2H), 4.70 (s, 2H), 3.51 – 3.39 (m, 6H), 3.06 – 2.95 (m, 6H), 2.56 (d, *J*=7.7 Hz, 4H), 2.27 (t, *J*=7.5 Hz, 4H), 1.96 (s, 3H), 1.56 – 1.42 (m, 6H), 1.42 – 1.30 (m, 6H), 1.30 – 1.17 (m, 6H). ^{13}C NMR (126 MHz, DMSO-d_6): δ 172.0, 171.3, 170.2, 169.1, 156.4, 147.7, 137.5, 117.4, 114.2, 50.7, 47.1, 46.8, 38.4, 38.3, 29.9, 28.8, 28.8, 27.6, 26.0, 23.5, 23.3, 20.4. HRMS: calculated for C$_{37}$H$_{57}$N$_9$O$_9$: 771.4279; found: 771.4283.

4.1.5. N-(2-(2-(2-(2-azidoethoxy)ethoxy)ethoxy)ethyl)-2-(di(pyridin-2-yl)amino)aceta-mide (12)

To a solution of acid **6** (501 mg, 1.9 mmol, 1 eq.) in DCM (90 mL), were added 2-(2-(2-(2-azidoethoxy)ethoxy)ethoxy)ethan-1-amine **11** (400 mg, 364 µL, 1.7 mmol, 0.95 eq.) and DIPEA (469 mg, 0.6 mL, 3.6 mmol, 2 eq.). Once the solid was completely dissolved, EDCI.HCl (696 mg, 3.6 mmol, 2 eq.) was added. The reaction mixture was stirred at 23 °C for 5 h, then adsorbed on silica and purified by chromatography on silica gel column (gradient EtOH in DCM, 0 % to 10 %) to give the expected product **12** isolated as a yellow oil (573 mg, 1.3 mmol, yield: 77 %). ^{1}H NMR (500 MHz, CDCl$_3$): δ 8.33 (ddd, *J*=4.9, 2.0, 0.9 Hz, 2H), 7.57 (ddd, *J*=8.4, 7.2, 2.0 Hz, 2H), 7.42 (bs, 1H), 7.16 (d, *J*=8.4 Hz, 2H), 6.92 (ddd, *J*=7.3, 4.9, 0.9 Hz, 2H), 4.74 (s, 2H), 3.63 (t, *J*=5.0 Hz, 2H), 3.62 – 3.56 (m, 4H), 3.52 – 3.39 (m, 8H), 3.35 (t, *J*=5.0 Hz, 2H). ^{13}C NMR (126 MHz, CDCl$_3$): δ 170.9, 156.7, 148.5, 137.8, 118.0, 114.6, 70.8, 70.7, 70.7, 70.4, 70.1, 70.0, 53.0, 50.8, 39.2. HRMS: calculated for C$_{20}$H$_{27}$N$_7$O$_4$: 429.2125; found: 429.2136.

4.1.6. Prop-2-yn-1-yl(3,14,25-trihydroxy-2,10,13,21,24-pentaoxo-3,9,14,20,25 pentaaza-tricontan-30-yl)carbamate (13)

To a solution of **7** (300 mg, 0.42 mmol, 1 eq.) in DMF (3 mL), was added DIPEA (235 mg, 300 µL, 1.82 mmol, 4,3 eq.). The reaction mixture was heated to 90 °C. Propargyl chloroformate (91 mg, 75 µL, 0.77 mmol, 1,8 eq.) was added in one portion. The reaction mixture was stirred at 90 °C for 5 min, then adsorbed on silica and purified by chromatography on silica gel column (gradient MeOH with 0,5 % H$_2$O in DCM, 0 % to 30 %) to give the expected product **13** isolated as a white solid (235 mg, 0.37 mmol, yield: 86 %). ^{1}H NMR (500 MHz, DMSO-d_6): δ 9.66 (s, 1H), 9.61 (s, 2H), 7.77 (t, *J*=4.9 Hz, 2H), 7.29 (t, *J*=5.7 Hz, 1H), 4.59 (d, *J*=2.5 Hz, 2H), 3.66 – 3.55 (m, 1H), 3.49 – 3.42 (m, 7H), 3.18 – 3.08 (m, 1H), 3.03 – 2.92 (m, 4H), 2.57 (t, *J*=7.5 Hz, 4H), 2.26 (t, *J*=7.4 Hz, 4H), 1.96 (s, 3H), 1.54 – 1.45 (m, 6H), 1.43 – 1.33 (m, 6H), 1.23 – 1.16 (m, 6H). ^{13}C NMR (126 MHz, DMSO-d_6): δ 172.0, 171.3, 170.1, 155.2, 76.9, 53.5, 51.3, 47.1, 46.8, 41.8, 40.3, 38.4, 29.9, 29.0, 28.8, 27.6, 26.0, 23.5, 23.3, 20.4. HRMS: calculated for C$_{29}$H$_{50}$N$_6$O$_{10}$: 642.3588; found: 642.3605.

4.1.7. (1-(1-(di(pyridin-2-yl)amino)-2-oxo-6,9,12-trioxa-3-azatetradecan-14-yl)-1H-1,2,3-triazol-4-yl)methyl(3,14,25-trihydroxy-2,10,13,21,24-pentaoxo-3,9,14,20,25-pentaazatriacontan-30-yl)carbamate (14)

To a solution of **13** (153 mg, 0.24 mmol, 0,96 eq.) in THF (7 mL), were added a solution of azide **12** (106 mg, 0.25 mmol, 1 eq.) in THF (7 mL) then water (7 mL). After 30 min at 24 °C, sodium ascorbate (144 mg, 0.73 mmol, 3 eq.) and aqueous saturated CuSO$_4$ solution (40 µL) were added. The reaction mixture was stirred at 24 °C for 20 h, then adsorbed on silica and purified by chromatography on silica gel column (gradient MeOH with 0,5 % H$_2$O in DCM, 0 % to 30 %). The purified fraction was precipitated in acetone to give the expected product **14** isolated as an off-white solid (112 mg, 0.10 mmol, yield: 44 %). ^{1}H NMR (500 MHz, DMSO-d_6): δ 9.73 (s, 1H), 9.67 (s, 2H), 8.28 – 8.25 (m, 2H), 8.05 (s, 1H), 7.92 (t, *J*=5.7 Hz, 1H), 7.79 (t, *J*=6.3 Hz, 2H), 7.65 (ddd, *J*=9.0, 7.2, 2.0 Hz, 2H), 7.20 (d, *J*=8.4 Hz, 2H), 7.17 (t, *J*=5.6 Hz, 1H), 6.96 (ddd, *J*=7.2, 4.9, 0.9 Hz, 2H), 5.01 (s, 2H), 4.72 (s, 2H), 4.50 (t,

J=5.2 Hz, 2H), 3.79 (t, J=5.2 Hz, 2H), 3.52 – 3.43 (m, 16H), 3.19 (q, J=5.8 Hz, 2H), 3.02 – 2.91 (m, 6H), 2.60 – 2.53 (m, 4H), 2.26 (t, J=7.4 Hz, 4H), 1.96 (s, 3H), 1.53 – 1.44 (m, 6H), 1.41 – 1.33 (m, 6H), 1.25 – 1.15 (m, 6H). ^{13}C NMR (126 MHz, DMSO-d_6): δ 172.0, 171.4, 170.2, 169.5, 156.4, 155.9, 147.8, 142.6, 137.6, 124.9, 117.4, 114.2, 69.7, 69.7, 69.6, 69.5, 69.0, 68.7, 56.9, 50.7, 49.4, 47.1, 46.8, 40.2, 38.6, 38.5, 30.0, 29.1, 28.8, 27.7, 26.1, 23.5, 23.4, 20.4. HRMS: calculated for $C_{49}H_{77}N_{13}O_{14}$: 1071.5713; found: 1071.5752.

4.1.8. Iridium(III) conjugate (10)

In a schlenk tube under inert atmosphere, iridium dimer [IrCl(piq)$_2$]$_2$ **9** (14 mg, 1.1x10^{-2} mmol, 1.0 eq.) and **8** (20 mg, 2.7x10^{-2} mmol, 2.2 eq.). were dissolved in 2:1 degassed solution of CH_2Cl_2/MeOH. The reaction mixture was stirred at 20 °C overnight. The mixture was evaporated under reduced pressure and purified by size exclusion column chromatography to give 27.2 mg of an orange solid was obtained (88 %). ^{1}H NMR (600 MHz, CDCl$_3$) δ 10.00 (br s, 1H), 9.84 (br s, 1H), 9.69 (br s, 1H), 8.88 (d, J=8.5 Hz, 2H), 8.73 (br s, 1H), 8.20 (d, J=8.0 Hz, 2H), 8.11 (br s, 2H), 8.00 (d, J=8.0 Hz, 2H), 7.79 (t, J=7.6 Hz, 2H), 7.74 (t, J=7.6 Hz, 4H), 7.63 – 7.52 (m, 8H), 7.02 (t, J=8.0 Hz, 2H), 6.78 (t, J=8.0 Hz, 2H), 6.74 (t, J=6.5 Hz, 2H), 6.28 (d, J=7.6 Hz, 2H), 4.90 (d, J=17.3 Hz, 1H), 4.59 (d, J=17.0 Hz, 1H), 3.75 – 3.53 (m, 6H), 3.34 – 3.22 (m, 2H), 3.21 – 3.11 (m, 4H), 2.93 – 2.77 (m, 4H), 2.66 – 2.47 (m, 4H), 2.09 (d, J=15.5 Hz, 3H), 1.74 – 1.54 (m, 8H), 1.53 – 1.42 (m, 6H), 1.35 – 1.18 (m, 4H) ppm. ^{13}C NMR (151 MHz, CDCl$_3$) δ 174.0, 173.3, 173.1, 172.3, 169.0, 168.0, 156.0, 153.0, 150.4, 145.6, 142.0, 140.3, 137.3, 132.4, 131.8, 130.8, 128.7, 127.8, 126.9, 126.5, 122.4, 121.5, 121.2, 118.1, 57.5, 47.4, 46.7, 39.3, 39.1, 38.9, 31.9, 31.6, 28.9, 28.6, 28.5, 28.4, 28.0, 26.2, 26.1, 25.5, 23.9, 23.5, 22.7, 20.9 ppm. HRMS calculated for $C_{67}H_{77}N_{11}O_9^{193}Ir$ ([M−Cl]$^+$), 1372.5525, found 1372.5535.

4.1.9. Iridium(III) conjugate (15)

In a schlenck tube under inert atmosphere, iridium dimer [IrCl(piq)$_2$]$_2$ **9** (17 mg, 1.3x10^{-2} mmol, 1.0 eq.) and **14** (30 mg, 2.8x10^{-2} mmol, 2.2 eq.). were dissolved in 2:1 degassed solution of CH_2Cl_2/MeOH. The reaction mixture was stirred at 20 °C overnight and purified by two consecutive size exclusion column chromatography to give 39.4 mg of an orange solid (88 %). ^{1}H NMR (600 MHz, CDCl$_3$) δ 10.01 (s, 1H), 9.77 (s, 1H), 9.67 (s, 1H), 8.95 (s, 1H), 8.88 (d, J=8.4 Hz, 2H), 8.20 (d, J=7.9 Hz, 2H), 8.12 (s, 2H), 8.03 – 7.97 (m, 2H), 7.96 (s, J=8.3 Hz, 1H), 7.79 (t, J=7.5 Hz, 2H), 7.76 – 7.72 (m, 4H), 7.61 – 7.53 (m, 8H), 7.02 (t, J=7.5 Hz, 2H), 6.78 (t, J=7.3 Hz, 2H), 6.76 – 6.71 (m, 2H), 6.27 (d, J=7.6 Hz, 2H), 6.08 (s, 1H), 5.12 (q, J=13.0 Hz, 2H), 4.93 (d, J=17.2 Hz, 1H), 4.64 (d, J=16.2 Hz, 1H), 4.57 – 4.48 (m, 2H), 3.86 (t, J=4.7 Hz, 2H), 3.60 (s, 16H), 3.46 (d, J=5.2 Hz, 2H), 3.15 (s, J=5.2 Hz, 4H), 3.09 (d, J=5.5 Hz, 2H), 2.84 – 2.75 (m, 4H), 2.58 (d, J=6.9 Hz, 4H), 2.12 (s, 3H), 1.67 – 1.53 (m, 6H), 1.53 – 1.36 (m, 6H), 1.34 – 1.18 (m, 6H) ppm. ^{13}C NMR (151 MHz, CDCl$_3$) δ 174.0, 173.9, 173.2, 172.9, 172.3, 169.0, 168.2, 156.0, 153.1, 150.4, 145.6, 142.1, 140.3, 137.3, 132.4, 131.8, 130.8, 130.4, 128.7, 128.5, 127.8, 126.9, 126.5, 125.1, 122.4, 121.4, 121.2, 118.1, 70.6, 70.5, 70.3, 69.5, 69.4, 57.9, 57.2, 50.4, 47.4, 47.2, 46.8, 40.7, 39.8, 39.5, 39.0, 38.8, 31.8, 31.6, 31.2, 28.7, 28.4, 28.2, 26.1, 26.0, 25.4, 23.7, 23.5, 23.2, 22.7, 20.9 ppm. HRMS calculated for $C_{79}H_{97}N_{15}O_{14}^{193}Ir$ ([M−Cl]$^+$), 1672.9494, found 1672.9506.

4.2. Physical chemistry

4.2.1. Absorbance and emission spectra

UV–visible absorption spectra were measured at room temperature in CH_2Cl_2 (1x10^{-5} mol.L^{-1} on a Perkin Elmer Lambda 40 UV–visible spectrometer; wavelengths are given in nm and extinction coefficient ε are presented in L.mol^{-1} cm^{-1} Emission spectra and luminescent quantum yields were recorded in dichloromethane solution (1x10^{-5} mol. L^{-1} on an Edinburgh Instrument FS5 Spectrofluorometer). The excited state lifetimes were recorded at room temperature in dichloromethane (1x10^{-5} mol.L^{-1} on a Horiba Scientific DeltaFlex TCSPC Spectrometer).

4.2.2. Cyclic voltammetry

Cyclic voltammetry experiments were carried out on an Autolab PGSTAT101 potentiostat unit from Metrohm with the Nova software package. A glassy carbon working electrode, a platinum wire auxiliary electrode and an Ag/AgCl (3 M KCl) as reference electrode were used in a standard three-electrode configuration. Cyclic voltammetry was performed in a 0.1 M anhydrous degassed solution of nBu$_4$NPF$_6$ in acetonitrile at a scanning rate of 0.1 V.s^{-1} Values were calibrated using ferrocene as reference.

4.3. Antimicrobial susceptibility testing

The strains used in this study are listed Table S1. The conditions used to determine the MICs of iridium complexes have been described recently by our group.[55] Briefly, 1.5 mL microtubes containing 100 μL of cation-adjusted Mueller Hinton broth (Becton, Dickinson and Company, Sparks, USA) or cation-adjusted, iron-depleted Mueller Hinton broth (iron concentration $\leq$ 0.03 mg/L) prepared as recommended by the CLSI,[52,56] were inoculated with 5 x 10^5 CFU of exponentially growing bacteria. The cultures were then incubated at 35 °C in a Plexiglass water-bath incubator (Dominique Dutscher, Bernolsheim, France) for 18 h $\pm$ 2 in the presence of log$_2$ increasing concentrations of iridium complex, in the dark (controls) and under blue LED light, respectively. The LED emitting at 473 nm with a power of 388 μW/cm^2 (RGB Flood Light B04-10 M−RGB, Meikee Lighting, Guandong, China) was placed vertically at 1 cm distance from the large side of the water-bath, as illustrated by Figure S25. The individual MIC values indicated in this work (lowest drug concentrations with no visible bacterial growth in the microtubes) correspond to the modal of at least three independent experiments.

4.4. Structural biology

4.4.1. Protein expression and purification

Recombinant FoxA (from *Pseudomonas aeruginosa*) was expressed and purified as previously described.[54] Briefly, C-terminal His$_6$-tagged protein was over-expressed in *Escherichia coli* Lemo21 strain with 0.5 mM L-rhamnose. Cells were grown at 37 °C to OD$_{600}$ of 1, temperature was lowered to 20 °C and expression was induced with 0.1 mM isopropyl-β-d-thiogalactopyranoside (IPTG) overnight. Cells were harvested, resuspended in buffer (30 mM Tris pH 7.4, 200 mM NaCl, 10 % glycerol) and lysed using a high-pressure homogenizer (EmulsiFlex-C3, Avestin). Cell debris was cleared by centrifugation at 22,000 g for 30 min and 1 % Triton X-100 was added to the supernatant and incubated for 1 hr at 4 °C. The insoluble outer membrane fraction was isolated by ultracentrifugation at 150,000 g and solubilized overnight with 1 % octyl glucopyranoside (OG). The solubilized material was cleared by centrifugation at 50,000 g and applied to Ni-NTA resin. The resin was washed with buffer supplemented with 0.4 % C8E4 and 25 mM imidazole, and the protein was eluted with 250 mM imidazole. Tobacco etch virus (TEV) protease was added to the eluted fraction (1:10 w/w) overnight followed by reverse Ni-NTA purification after removal of imidazole. The purified protein was concentrated and further purified using size-exclusion chromatography (Superdex S200 10/300 column).

4.4.2. Crystallization and structure determination

For crystallization, FoxA (7–10 mg/ml) was mixed with 3–4 fold excess ligand (compound **8** /compound **14**/compound **15**) dissolved in 100 % DMSO and incubated on ice for approximately 30 min. Crystals of FoxA-**8** and FoxA-**14** complex were grown in 2.1–2.4 M ammonium sulfate, 0.1 M HEPES pH 7, 0.05 M NaCl, 0.7 % β-octyl glucopyranoside. Crystals of FoxA-**15** complex were grown in 2.4 M Ammonium sulphate, 0.1 M Tris pH 8, 0.7 % β-octyl glucopyranoside. All crystals appeared after 3–5 days, grew to 20–100 μm maximum size and were cryo-protected with step-wise addition of glycerol to a final concentration of 20 % (v/v) followed by immediate harvest.

X-ray diffraction data were collected at the P14 beamline at EMBL,

Hamburg. All data were processed with XDS[57] and reduced with AIMLESS.[58,59] The StarANISO server[60] was used to perform anisotropy correction of the data. The structure was solved using molecular replacement in Phaser[61] using apo FoxA (pdb: 6I96) as a search model and refined using REFMAC5 and Phenix.Refine[62,63] to 2.22 Å (compound **8**) and 2.48 Å (compound **14**). All data collection and refinement statistics are summarized in Table S4. Coordinates have been deposited to the Protein Data Bank (pdb: 8RM3 / 8RMI). Figures were prepared using Pymol and UCSF Chimera.

CRediT authorship contribution statement

Aline Faucon: Investigation. **Julien Renault:** Investigation. **Inokentijs Josts:** Writing – review & editing, Writing – original draft, Investigation. **Julie Couchot:** Investigation. **Jean-Luc Renaud:** Writing – review & editing, Writing – original draft, Validation, Conceptualization. **Françoise Hoegy:** Investigation. **Patrick Plésiat:** Writing – review & editing, Writing – original draft, Validation, Supervision, Methodology, Funding acquisition. **Henning Tidow:** Writing – review & editing, Writing – original draft, Validation, Supervision. **Sylvain Gaillard:** Writing – review & editing, Writing – original draft, Supervision, Project administration, Methodology, Funding acquisition, Conceptualization. **Gaëtan L.A. Mislin:** Writing – review & editing, Writing – original draft, Supervision, Project administration, Methodology, Funding acquisition, Conceptualization.

Declaration of competing interest

The authors declare that they have no known competing financial interests or personal relationships that could have appeared to influence the work reported in this paper.

Data availability

Data will be made available on request.

Acknowledgements

Authors contributions

GLAM, PP, SG and JLR. wrote the manuscript with inputs from the other authors. GLAM supervised organic chemistry experiments. SG and JLR. supervised organometallic chemistry experiments. PP supervise microbiology experiments. ALF prepared compounds **6**, **8**, **12**, **13** and **14**. FH scaled up the synthesis. JR synthesized, purified and characterized iridium compounds **9**, **10** and **16**. JC performed antibiotic assays under the supervision of PP. GLAM, SG and PP found the grants. IJ performed structural biology experiments (purification of FoxA, co-crystallization, structure determination) supervised by HT.

Appendix A. Supplementary data

Supplementary data to this article can be found online at https://doi.org/10.1016/j.bmc.2024.117842.

References

1. Piddock LJV. Reflecting on the Final Report of the O'Neill Review on Antimicrobial Resistance. *Lancet Infect Dis.* 2016;16:767–768. https://doi.org/10.1016/S1473-3099(16)30127-X.
2. Wells V, Piddock LJV. Addressing Antimicrobial Resistance in the UK and Europe. *Lancet Infect Dis.* 2017;17:1230–1231. https://doi.org/10.1016/S1473-3099(17)30633-3.
3. Micoli F, Bagnoli F, Rappuoli R, Serruto D. The Role of Vaccines in Combatting Antimicrobial Resistance. *Nat Rev Microbiol.* 2021;19:287–302. https://doi.org/10.1038/s41579-020-00506-3.
4. Uyttebroek S, Chen B, Onsea J, et al. Safety and Efficacy of Phage Therapy in Difficult-to-Treat Infections: A Systematic Review. *Lancet Infect Dis.* 2022;22:e208–e220. https://doi.org/10.1016/S1473-3099(21)00612-5.
5. Kouijzer JJP, Lattwein KR, Beekers I, et al. Vancomycin-Decorated Microbubbles as a Theranostic Agent for Staphylococcus Aureus Biofilms. *Int J Pharm.* 2021;609, 121154. https://doi.org/10.1016/j.ijpharm.2021.121154.
6. *Ueber die Wirkung fluorescirender Stoffe auf Infusorien / von Oscar Raab.* Wellcome Collection. https://wellcomecollection.org/works/fmjywnqn (accessed 2023-12-14).
7. Yin R, Dai T, Avci P, et al. Light Based Anti-Infectives: Ultraviolet C Irradiation, Photodynamic Therapy, Blue Light, and Beyond. *Curr Opin Pharmacol.* 2013;13:731–762. https://doi.org/10.1016/j.coph.2013.08.009.
8. Tornaletti S, Pfeifer GP. UV Damage and Repair Mechanisms in Mammalian Cells. *Bioessays.* 1996;18:221–228. https://doi.org/10.1002/bies.950180309.
9. Wegener M, Hansen MJ, Driessen AJM, Szymanski W, Feringa BL. Photocontrol of Antibacterial Activity: Shifting from UV to Red Light Activation. *J Am Chem Soc.* 2017;139:17979–17986. https://doi.org/10.1021/jacs.7b09281.
10. Frei A, Verderosa AD, Elliott AG, Zuegg J, Blaskovich MAT. Metals to Combat Antimicrobial Resistance. *Nat Rev Chem.* 2023;7:202–224. https://doi.org/10.1038/s41570-023-00463-4.
11. Frei A, Zuegg J, Elliott AG, et al. Metal Complexes as a Promising Source for New Antibiotics. *Chem Sci.* 2020;11:2627–2639. https://doi.org/10.1039/c9sc06460e.
12. Patra M, Gasser G, Metzler-Nolte N. Small Organometallic Compounds as Antibacterial Agents. *Dalton Trans.* 2012;41:6350–6358. https://doi.org/10.1039/C2DT12460B.
13. Nikaido H. Molecular Basis of Bacterial Outer Membrane Permeability Revisited. *Microbiol Mol Biol Rev.* 2003;67:593–656. https://doi.org/10.1128/MMBR.67.4.593-656.2003.
14. Krewulak KD, Vogel HJ. Structural Biology of Bacterial Iron Uptake. *BBA.* 2008;1778:1781–1804. https://doi.org/10.1016/j.bbamem.2007.07.026.
15. Hider RC, Kong X. Chemistry and Biology of Siderophores. *Nat Prod Rep.* 2010;27:637–657. https://doi.org/10.1039/b906679a.
16. Schalk IJ, Mislin GLA, Brillet K. Structure, Function and Binding Selectivity and Stereoselectivity of Siderophore-Iron Outer Membrane Transporters. *Curr Top Membr.* 2012;69:37–66. https://doi.org/10.1016/B978-0-12-394390-3.00002-1.
17. Celia H, Noinaj N, Buchanan SK. Structure and Stoichiometry of the Ton Molecular Motor. *Int J Mol Sci.* 2020;21:375. https://doi.org/10.3390/ijms21020375.
18. Schalk IJ, Guillon L. Fate of Ferrisiderophores after Import across Bacterial Outer Membranes: Different Iron Release Strategies Are Observed in the Cytoplasm or Periplasm Depending on the Siderophore Pathways. *Amino Acids.* 2013;44:1267–1277. https://doi.org/10.1007/s00726-013-1468-2.
19. Hannauer M, Barda Y, Mislin GLA, Shanzer A, Schalk IJ. The Ferrichrome Uptake Pathway in Pseudomonas Aeruginosa Involves an Iron Release Mechanism with Acylation of the Siderophore and Recycling of the Modified Desferrichrome. *J Bacteriol.* 2010;192:1212–1220. https://doi.org/10.1128/JB.01539-09.
20. Imperi F, Tiburzi F, Visca P. Molecular Basis of Pyoverdine Siderophore Recycling in Pseudomonas Aeruginosa. *Proc Natl Acad Sci.* 2009;106:20440–20445. https://doi.org/10.1073/pnas.0908760106.
21. Ferguson AD, Hofmann E, Coulton JW, Diederichs K, Welte W. Siderophore-Mediated Iron Transport: Crystal Structure of FhuA with Bound Lipopolysaccharide. *Science.* 1998;282:2215–2220. https://doi.org/10.1126/science.282.5397.2215.
22. Thomas X, Destoumieux-Garzón D, Peduzzi J, et al. Siderophore Peptide, a New Type of Post-Translationally Modified Antibacterial Peptide with Potent Activity. *J Biol Chem.* 2004;279:28233–28242. https://doi.org/10.1074/jbc.M400228200.
23. Sato T, Yamawaki K. Cefiderocol: Discovery, Chemistry, and In Vivo Profiles of a Novel Siderophore Cephalosporin. *Clin Infect Dis.* 2019;69:S538–S543. https://doi.org/10.1093/cid/ciz826.
24. Rayner B, Verderosa AD, Ferro V, Blaskovich MAT. Siderophore Conjugates to Combat Antibiotic-Resistant Bacteria. *RSC Med Chem.* 2023;14:800–822. https://doi.org/10.1039/d2md00465h.
25. Mislin GLA, Schalk IJ. Siderophore-Dependent Iron Uptake Systems as Gates for Antibiotic Trojan Horse Strategies against Pseudomonas Aeruginosa. *Metallomics.* 2014;6:408–420. https://doi.org/10.1039/c3mt00359k.
26. Dassonville-Klimpt A, Sonnet P. Advances in 'Trojan Horse' Strategies in Antibiotic Delivery Systems. *Future Med Chem.* 2020;12:983–986. https://doi.org/10.4155/fmc-2020-0065.
27. Górska A, Sloderbach A, Marszałł MP. Siderophore-Drug Complexes: Potential Medicinal Applications of the "Trojan Horse" Strategy. *Trends Pharmacol Sci.* 2014;35:442–449. https://doi.org/10.1016/j.tips.2014.06.007.
28. *Organometallics.* 2018;37:915–923. https://doi.org/10.1021/acs.organomet.7b00885.
29. Guo C, Nolan EM. Heavy-Metal Trojan Horse: Enterobactin-Directed Delivery of Platinum(IV) Prodrugs to Escherichia Coli. *J Am Chem Soc.* 2022;144:12756–12768. https://doi.org/10.1021/jacs.2c03324.

30. Southwell JW, Herman R, Raines DJ, et al. Siderophore-Linked Ruthenium Catalysts for Targeted Allyl Ester Prodrug Activation within Bacterial Cells. *Chemistry – A. European Journal.* 2023;29:e202202536.

31. Youf R, Nasir A, Müller M, et al. Ruthenium(II) Polypyridyl Complexes for Antimicrobial Photodynamic Therapy: Prospects for Application in Cystic Fibrosis Lung Airways. *Pharmaceutics.* 2022;14:1664. https://doi.org/10.3390/pharmaceutics14081664.

32. Ng XY, Fong KW, Kiew LV, et al. Ruthenium(II) Polypyridyl Complexes as Emerging Photosensitisers for Antibacterial Photodynamic Therapy. *J Inorg Biochem.* 2024; 250, 112425. https://doi.org/10.1016/j.jinorgbio.2023.112425.

33. Heinemann F, Karges J, Gasser G. Critical Overview of the Use of Ru(II) Polypyridyl Complexes as Photosensitizers in One-Photon and Two-Photon Photodynamic Therapy. *Acc Chem Res.* 2017;50:2727–2736. https://doi.org/10.1021/acs.accounts.7b00180.

34. Sauvageot E, Elie M, Gaillard S, et al. Antipseudomonal Activity Enhancement of Luminescent Iridium(Iii) Dipyridylamine Complexes under Visible Blue Light. *Metallomics.* 2017;9:1820–1827. https://doi.org/10.1039/c7mt00262a.

35. Walker JR, Altman E. Biotinylation Facilitates the Uptake of Large Peptides by Escherichia Coli and Other Gram-Negative Bacteria. *Appl Environ Microbiol.* 2005;71: 1850–1855. https://doi.org/10.1128/AEM.71.4.1850-1855.2005.

36. Farkas E, Enyedy ÉA, Csóka H. A Comparison between the Chelating Properties of Some Dihydroxamic Acids. *Desferrioxamine B and Acetohydroxamic Acid. Polyhedron.* 1999;18:2391–2398. https://doi.org/10.1016/S0277-5387(99)00144-8.

37. Llamas MA, Sparrius M, Kloet R, Jiménez CR, Vandenbroucke-Grauls C, Bitter W. The Heterologous Siderophores Ferrioxamine B and Ferrichrome Activate Signaling Pathways in Pseudomonas Aeruginosa. *J Bacteriol.* 2006;188:1882–1891. https://doi.org/10.1128/jb.188.5.1882-1891.2006.

38. Normant V, Josts I, Kuhn L, et al. Nocardamine-Dependent Iron Uptake in Pseudomonas Aeruginosa: Exclusive Involvement of the FoxA Outer Membrane Transporter. *ACS Chem Biol.* 2020;15:2741–2751. https://doi.org/10.1021/acschembio.0c00535.

39. Chan DCK, Burrows LL. Pseudomonas Aeruginosa FpvB Is a High-Affinity Transporter for Xenosiderophores Ferrichrome and Ferrioxamine B. *MBio.* 2022;14: e03149–e10222. https://doi.org/10.1128/mbio.03149-22.

40. Josts I, Veith K, Normant V, Schalk IJ, Tidow H. Structural Insights into a Novel Family of Integral Membrane Siderophore Reductases. *Proc Natl Acad Sci.* 2021;118. https://doi.org/10.1073/pnas.2101952118. e2101952118.

41. Kirin SI, Yennawar HP, Williams ME. Synthesis and Characterization of CuII Complexes with Amino Acid Substituted Di(2-Pyridyl)Amine Ligands. *Eur J Inorg Chem.* 2007;2007:3686–3694. https://doi.org/10.1002/ejic.200700273.

42. Faucon AL, Hoegy F, Werle N, Gourlaouen C, Mislin GLA. Dipyridylamine-Acetamide (Dpaa): A Primary Amine Protecting Group Orthogonally Cleavable under Acidic Conditions in the Presence of t-Butyloxycarbonyl (Boc) and t-Butylester. *Tetrahedron Lett.* 2022;96, 153758. https://doi.org/10.1016/j.tetlet.2022.153758.

43. Liang L, Astruc D. The Copper(I)-Catalyzed Alkyne-Azide Cycloaddition (CuAAC) "Click" Reaction and Its Applications. *An Overview. Coordination Chemistry Reviews.* 2011;255:2933–2945. https://doi.org/10.1016/j.ccr.2011.06.028.

44. Tornøe CW, Christensen C, Meldal M. Peptidotriazoles on Solid Phase: [1,2,3]-Triazoles by Regiospecific Copper(I)-Catalyzed 1,3-Dipolar Cycloadditions of Terminal Alkynes to Azides. *J Org Chem.* 2002;67:3057–3064. https://doi.org/10.1021/jo011148j.

45. Rostovtsev VV, Green LG, Fokin VV, Sharpless KB. A Stepwise Huisgen Cycloaddition Process: Copper(I)-Catalyzed Regioselective "Ligation" of Azides and Terminal Alkynes. *Angew Chem Int Ed.* 2002;41:2596–2599. https://doi.org/10.1002/1521-3773(20020715)41:14<2596::AID-ANIE2596>3.0.CO;2-4.

46. Liu S-J, Zhao Q, Fan Q-L, Huang W. A Series of Red-Light-Emitting Ionic Iridium Complexes: Structures, Excited State Properties, and Application in Electroluminescent Devices. *Eur J Inorg Chem.* 2008;2008:2177–2185. https://doi.org/10.1002/ejic.200701184.

47. Slinker JD, Gorodetsky AA, Lowry MS, et al. Efficient Yellow Electroluminescence from a Single Layer of a Cyclometalated Iridium Complex. *J Am Chem Soc.* 2004;126: 2763–2767. https://doi.org/10.1021/ja0345221.

48. Lowry MS, Goldsmith JI, Slinker JD, et al. Single-Layer Electroluminescent Devices and Photoinduced Hydrogen Production from an Ionic Iridium(III) Complex. *Chem Mater.* 2005;17:5712–5719. https://doi.org/10.1021/cm051312+.

49. Lowry MS, Goldsmith JI, Slinker JD, Jr PRA, Malliaras GG, Bernhard S. Correction to Single-Layer Electroluminescent Devices and Photoinduced Hydrogen Production from an Ionic Iridium(III) Complex. *Chem Mater.* 2023;35:1466. https://doi.org/10.1021/acs.chemmater.2c03710.

50. Bevernaegie R, Wehlin SAM, Elias B, Troian-Gautier L. A Roadmap Towards Visible Light Mediated Electron Transfer Chemistry with Iridium(III) Complexes. *ChemPhotoChem.* 2021;5:217–234. https://doi.org/10.1002/cptc.202000255.

51. Huang H, Banerjee S, Sadler PJ. Recent Advances in the Design of Targeted Iridium (III) Photosensitizers for Photodynamic Therapy. *Chembiochem.* 2018;19: 1574–1589. https://doi.org/10.1002/cbic.201800182.

52. Clinical and Laboratory Standards Institute. Performance Standards for Antimicrobial Susceptibility Testing, 30th edition (supplement M100), 2020, Wayne, PA, USA.

53. Chan DCK, Josts I, Koteva K, Wright GD, Tidow H, Burrows LL. Interactions of TonB-Dependent Transporter FoxA with Siderophores and Antibiotics That Affect Binding, Uptake, and Signal Transduction. *PNAS.* 2023;120. https://doi.org/10.1073/pnas.2221253120. e2221253120.

54. Josts I, Veith K, Tidow H. Ternary Structure of the Outer Membrane Transporter FoxA with Resolved Signalling Domain Provides Insights into TonB-Mediated Siderophore Uptake. *Elife.* 2019;8:e48528.

55. Renault J, Couchot J, Faucon AL, et al. 2-Thiophenyl–isoquinoline Ir(III) complex: A promising tool in antipseudomonal photodynamic therapy under red irradiation. *Eur J Inorg Chem.* 2024;27:e202300767.

56. Clinical and Laboratory Standards Institute. Methods for dilution antimicrobial susceptibility tests for bacteria that grow aerobically, approved standard, 7th edition (document M7–A7, vol. 26, no 2), 2006, Wayne, PA, USA.

57. Kabsch WXDS. *Acta Crystallogr D Biol Crystallogr.* 2010;66:125–132. https://doi.org/10.1107/S0907444909047337.

58. Evans P. Scaling and Assessment of Data Quality. *Acta Crystallogr D Biol Crystallogr.* 2006;62:72–82. https://doi.org/10.1107/S0907444905036693.

59. Evans PR. An Introduction to Data Reduction: Space-Group Determination, Scaling and Intensity Statistics. *Acta Crystallogr D Biol Crystallogr.* 2011;67:282–292. https://doi.org/10.1107/S090744491003982X.

60. Tickle IJ, Flensburg C, Keller P, et al. STARANISO. Cambridge, United Kingdom: Global Phasing Ltd.; 2018.

61. McCoy AJ, Grosse-Kunstleve RW, Adams PD, Winn MD, Storoni LC, Read RJ. Phaser Crystallographic Software. *J Appl Cryst.* 2007;40:658–674. https://doi.org/10.1107/S0021889807021206.

62. Murshudov GN, Skubák P, Lebedev AA, et al. REFMAC5 for the Refinement of Macromolecular Crystal Structures. *Acta Crystallogr D Biol Crystallogr.* 2011;67: 355–367. https://doi.org/10.1107/S0907444911001314.

63. Afonine PV, Grosse-Kunstleve RW, Echols N, et al. Towards Automated Crystallographic Structure Refinement with Phenix.Refine. *Acta Crystallogr. D Biol. Crystallogr.* 2012;68:352–367. https://doi.org/10.1107/S0907444912001308.